Novel Boron Nitride Hollow Nanoribbons

Zhi-Gang Chen,[†,‡] Jin Zou,[§] Gang Liu,[†] Feng Li,[†] Yong Wang,[§] Lianzhou Wang,[‡] Xiao-Li Yuan,[¶] Takashi Sekiguchi,[¶] Hui-Ming Cheng,[†,*] and Gao Qing Lu[‡,*]

[†]Shenyang National Laboratory for Materials Science, Institute of Metal Research, Chinese Academy of Sciences, Shenyang 110016, China, [‡]ARC Centre of Excellence for Functional Nanomaterials, School of Engineering and AIBN, The University of Queensland, Brisbane QLD 4072, Australia, [§]School of Engineering and Centre for Microscopy and Microanalysis, The University of Queensland, Brisbane QLD 4072, Australia, and [¶]Advanced Electronic Materials Center, National Institute for Materials Science, 1-1 Namiki, Tsukuba 305-0044, Japan

ABSTRACT Novel BN hollow nanoribbons (BNHNRs) were fabricated by a simple ZnS nanoribbon templating method. Such BNHNRs have a distinct structure and show unique optical properties, as demonstrated from Raman, Fourier transform infrared spectroscopy, UV—vis spectroscopy, and cathodoluminescence spectroscopy, when compared with other forms of BN nanostructures. With high crystallinity, the BNHNRs exhibit an extraordinary ultraviolet CL emission at 5.33 eV. Such a property is highly advantageous for optoelectronic applications, particularly in the ultraviolet region, such as blue lasing and light emitting diodes. This templating method has also been extended to synthesize other hollow nanostructures such as boron carbonitride. This study represents a new methodology for fabricating hollow nanostructures with defined crystallinity and unique optical properties.

KEYWORDS: BN · hollow nanostructures · nanoribbons · ZnS · cathodoluminescence

Since the discovery of carbon nanotubes,[1] one-dimensional (1D) nanomaterials have drawn extensive attention as potential building blocks for future nano/microscaled devices.[2] Various 1D nanostructures, such as tube-like,[3−6] wire-like,[7] and ribbon-like structures,[8,9] have been studied extensively. Geometrically, 1D nanostructures can be classified into two main categories: one has an elongated rectangular cross section, such as ribbons/belts, and the other has an axial equalized symmetric cross section, such as tubes and wires. Among them, hollow nanostructures have important applications as optoelectronic devices and/or nanoscale reactors for catalysis, drug delivery, separation, storage, and nanoencapsulation.[5,10−14] To date, hard templating[15] methods have been developed for the synthesis of various hollow nanostructures including metals,[16] semiconductors,[17] polymers,[18] and carbon.[19] Soft templates[20,21] and the Kirkendall effect[22] have also been widely used to fabricate desired hollow nanostructures with controlled morphology. In this study, we demonstrate, for the first time, the synthesis of boron nitride hollow nanoribbons (BNHNRs) through a simple method using ZnS nanoribbons as template. The synthesized BNHNRs replicate precisely the morphologies of the ZnS template and exhibit ultraviolet optical properties.

As a wide band gap semiconductor, BN and its associated low dimensional nanostructures have continuously attracted wide interest due to their structure-independent band gap.[23] In particular, BN nanomaterials have excellent optical[24] and mechanical[25] properties, high thermal conductivity,[26] resistance to oxidation,[27] and chemical inertness.[28] In addition, a recent theoretical study predicted the existence of piezoelectric behavior in BN nanotubes due to the polar nature of B−N chemical bond.[29] BN nanostructures thus have a great potential as unique electromechanical and optoelectronic components. Although various BN nanostructures, such as nanotubes (NTs),[30,31] nanobamboos,[32] yard-glass shaped BNNTs,[33] nanohorns,[34] nanowires,[35] core/shell heterostructures,[36] have been synthesized, to our best knowledge, no hollow BN nanoribbons have been reported so far.

In order to synthesize BNHNRs and to evaluate the synthesis strategy and the quality of synthesized BNHNRs, the choice of an appropriate templating material is essential. In this study, we chose ZnS as template for the following reasons:

- ZnS nanoribbons can be easily synthesized by chemical vapor deposition.[37,38]
- The polar nature[39] of ZnS may lead to asymmetric growth and form nanoribbons with distinct edges, that is, one is straight and the other is zigzag.[40] This is critically important to evaluate whether template structures can be precisely replicated during the fabrication.

*Address correspondence to cheng@imr.ac.cn, maxlu@uq.edu.au.

Received for review August 4, 2008 and accepted September 19, 2008.

Published online October 2, 2008.
10.1021/nn8004922 CCC: $40.75

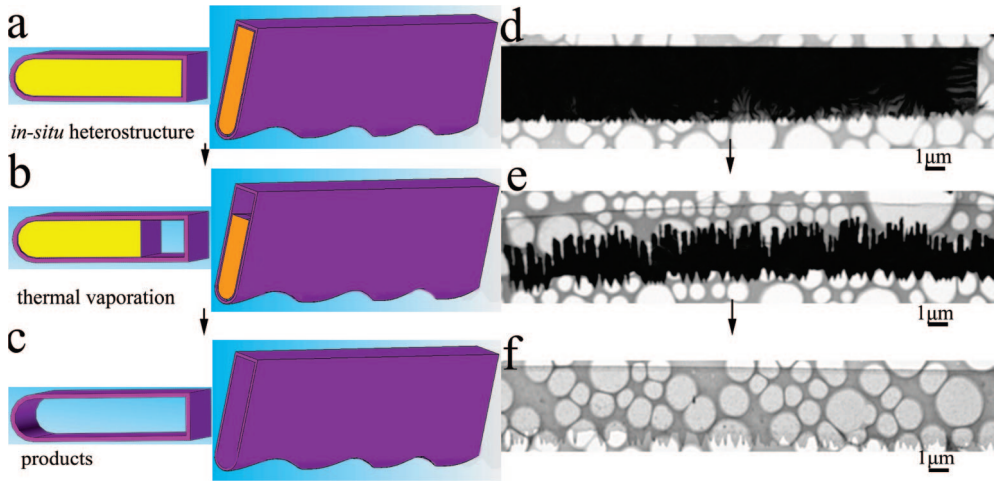

Figure 1. Schematic of this synthesis strategy. (a) Cross section and section of ZnS/BN belt heterostructure. (b) Intermediate heterostructure following partial vaporization. (c) Hollow BN nanostructure. (d−f) TEM images of the synthesized products confirming these illustrated structural characteristics.

- Under H_2, ZnS vaporizes at 1100 °C[41] while BN does not vaporize until 3000 °C, so that replicated BN can be preserved when the ZnS template is removed by vaporization.
- Both ZnS and BN have a hexagonal structure.
- Importantly, ZnS nanoribbons can be synthesized in a large quantity,[41] so that it is possible to scale-up this process to produce a large amount of BNHNRs.

RESULTS AND DISCUSSION

Figure 1a−c is the schematic illustration of the synthesis strategy, in which ZnS/BN core/shell heterostructures (Figure 1a) were initially formed by coating a layer of BN honeycomb sheets over the entire surface of asymmetrically grown ZnS nanoribbons, followed by thermal evaporation of ZnS (Figure 1b shows an intermediate step) that results in BN hollow nanoribbons (Figure 1c). The synthesized BNHNRs exhibit the same morphology as the original ZnS nanoribbons but in a hollow form. This synthesis strategy has been experimentally realized, as evidenced by transmission electron microscopy (TEM) observations in Figure 1d−f.

Figure 2a−d is the typical scanning electron microscopy (SEM) images of the synthesized products taken at different magnifications, showing the general morphological characteristics, from which a large quantity of belt-like structures can be clearly observed. Extensive SEM investigations show the following three characteristics: (1) the length of these structures is in the range of several tens of micrometers; (2) their cross section is also belt-shaped with a typical width of 5−10 μm and a thickness of ~150 nm (Figure 2b,c); (3) their broken cross section displays a hollow morphology (Figure 2d). Their X-ray diffraction (XRD) pattern, as shown in Figure 2e, indicates a hexagonal (h-) BN with the lattice parameters of $a = 0.250$ nm and $c = 0.665$ nm. The fact that no other diffraction peaks were observed indicates that the synthesized product has an extremely high purity of BN without impurities, such as ZnS, Zn, and S crystalline phases.

To confirm the hollow morphology and structural/chemical characteristics of synthesized structures, extensive TEM investigations were carried out. Figure 3a,b shows TEM images taken from a section of a typical synthesized BN nanostructure with different viewing directions. The two long edges are shown differently with one being zigzag and the other being straight. As can be seen from the tilted image (Figure 3b, tilted by ~45°), a double-line profile parallel to the straight edge is observed, indicating that the straight edge must be thick. However, this is not the case for the zigzag edge. This implies that the cross-section of the BN nanostructure has a hollow belt form, as illustrated in Figure 1c. To determine their crystallographic nature, selected area electron diffraction (SAED) was carried out. Figure 3c,d is the SAED patterns taken from regions containing the middle and the straight edge, as marked in Figure 3a. Figure 3c shows a pair of diffraction rings with arcs of $10\bar{1}0$* diffractions and arcs of $11\bar{2}0$* diffractions. No ±0002* diffractions can be observed in Figure 3c, indicating that the electron beam is parallel to the normal of BN graphene-like sheets. It is of interest to note that these BN sheets give rise to arc formed diffractions, implying that they have a preferred orientation. On the other hand, Figure 3d shows ±0002* diffraction spots (with slightly arced) superimposed with the diffraction pattern given by Figure 3c, suggesting that the ±0002* diffraction spots must result from the vertically aligned BN graphite-like sheets that are parallel to the straight edge. To confirm this, high resolution (HR) TEM was conducted. Figure 3e is a typical HRTEM image of the straight edge, showing the wall structure of the layered BN sheets, in which a wall thickness of ~12 nm consisting of about 35 graphene-like sheets is clearly seen. The wall is high-crystallized with the identical lattice spacing of ~0.33 nm (corresponding to d_{0002} of h-BN).

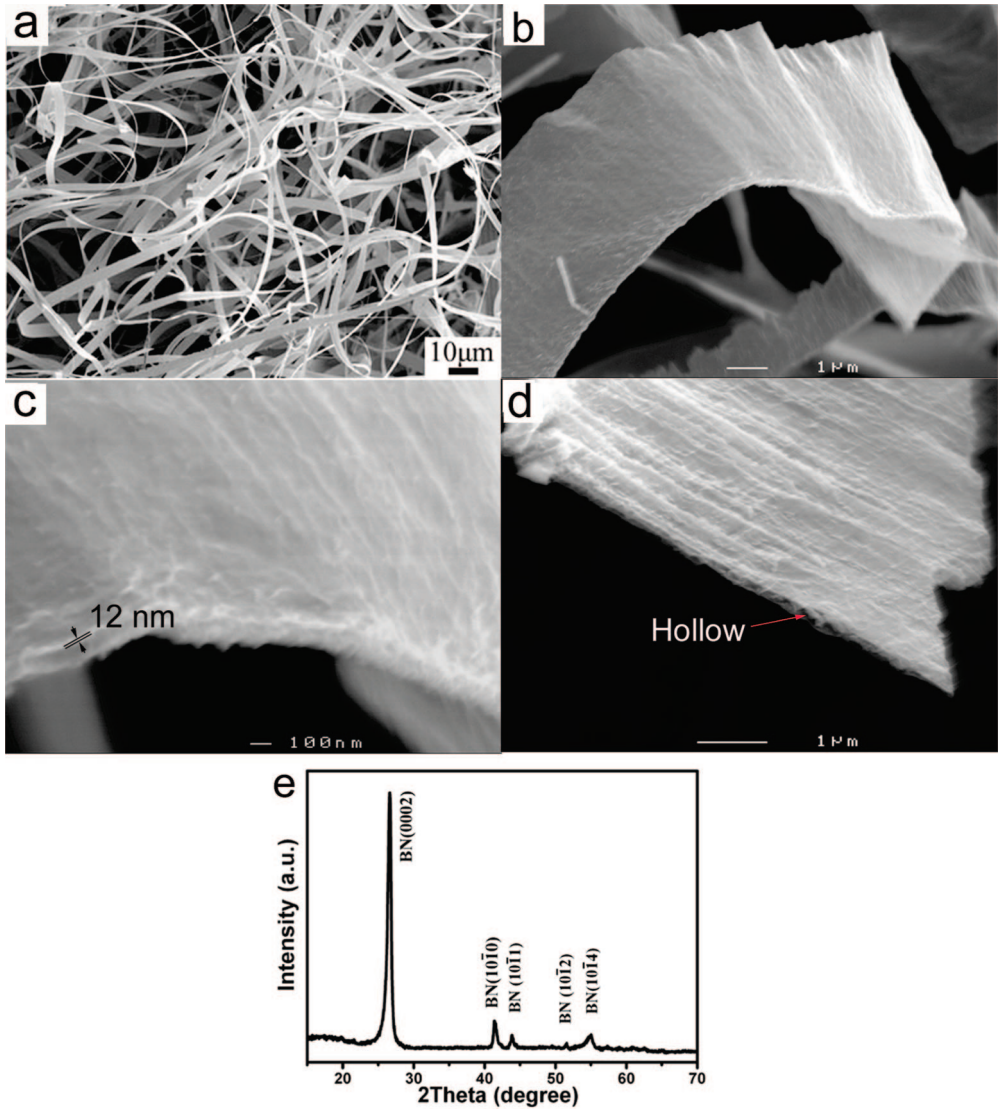

Figure 2. (a) Low magnification SEM image showing high density of synthesized BN products. (b−d) High magnification SEM images of a synthesized BN product showing their typical thickness and hollow characteristic. (e) XRD pattern of the synthesized BN products.

The *in-plane* [(10$\bar{1}$0) planes] lattice spacing can also be measured from HRTEM images to be ~0.22 nm (Figure 3e). Such results indicate that these sheets have high crystallinity. By carefully analyzing the 10$\bar{1}$0* arcs with 0002* arced spots shown in Figure 3d, we note that two of the 10$\bar{1}$0* arcs have their maxima parallel to the 0002* arced spots. This suggests that most of <10$\bar{1}$0> directions in the flat BN graphite-like sheets are parallel to the normal of BN sheets in the vertical section of the straight edge. Furthermore, two of the 11$\bar{2}$0* arcs have their maxima parallel to the long axis of the BNHNR, indicating that the BNHNRs have their axial directions parallel to <11$\bar{2}$0>. Figure 3f is a typical HRTEM image of the zigzag edges, which shows a curved shape of BN sheets, indicating good replication of BNHNRs from the ZnS template nanostructures. To determine their chemical composition, energy filtered (EF) TEM was used to show elemental maps of B, N, and C. Images were formed with the energy loss windows centered, respectively, at the B *K* edge of 188 eV, the N *K* edge of 401 eV, and the C *K* edge of 284 eV, and with slit sizes of 10, 20, and 16 eV, respectively. Figure 3g is an image using electrons with the zero energy loss showing the general morphology of a section of a BNHNR. Figure 3h,i shows B and N maps of the section and clearly show the presence of B and N. Figure 3j is a C map, in which the holey C film is clearly shown. However, the disappearance of C signal in the BNHNR section and the decreased intensity in the overlapping region between the BNHNR and C film (due to the multiple scattering effect) in Figure 3j suggest that the BNHNR contains B and N only. Figure 3k is the overlapped image of B, C, and N maps. To further confirm the structure of BNHNRs and the absence of C in the hollow BN nanostructures, electron energy loss spectroscopy (EELS) was used. Figure 3l is a typical EELS profile and shows sharp π^* peaks on the left sides of both B and N *K* edges, indicating that the BNHNRs have

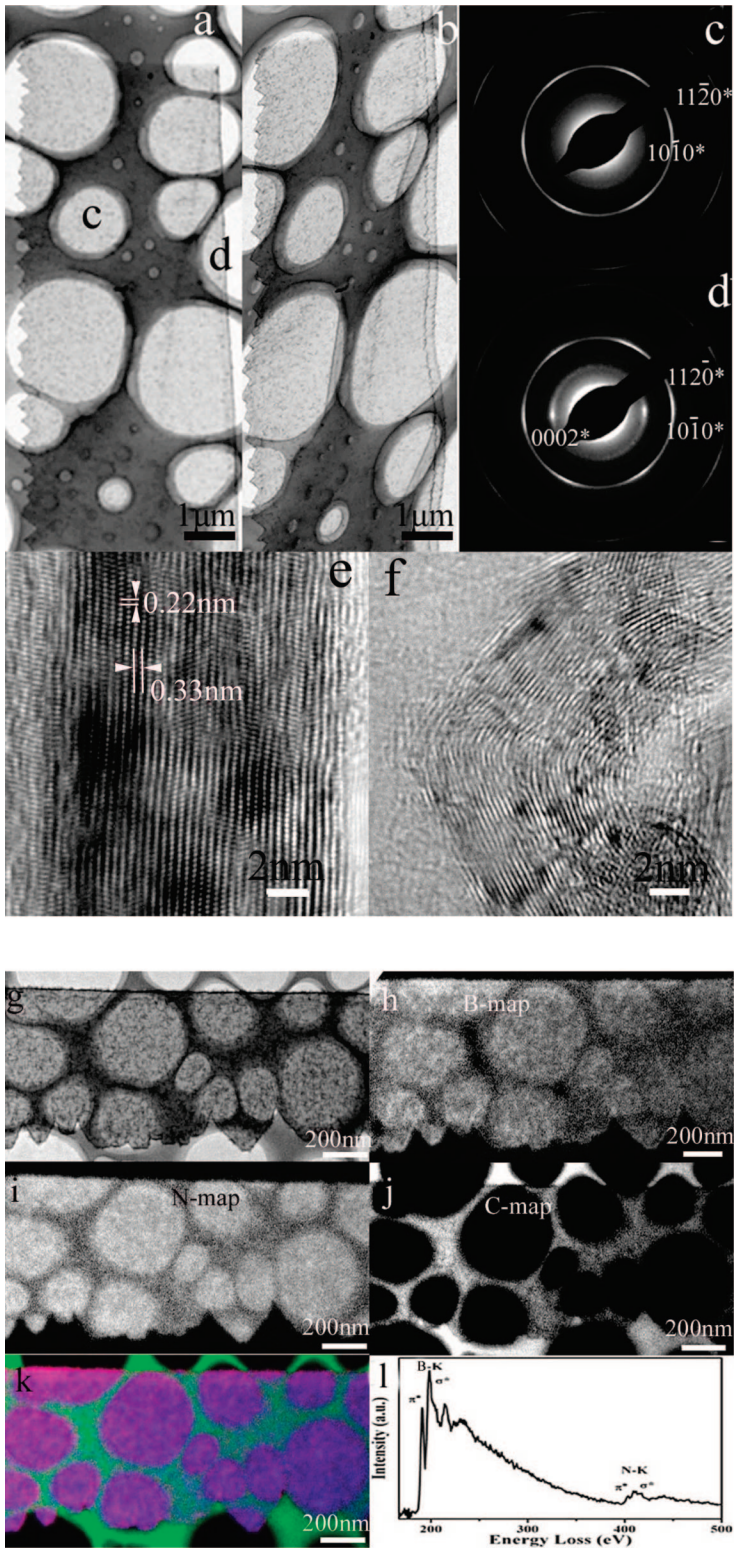

Figure 3. (a,b) TEM images of a section of BNHNR with (a) viewed from the top and (b) viewed from the tilted sample. (c,d) SAED patterns taken from the middle of the BNHNR (c) and the straight edge of the BNHNR (d). (e,f) HR-TEM images of straight edge and zigzag edge, respectively. (g) Zero-loss image of a section of BNHNR; (h−j) Elemental maps (B, N, and C) of the BNHNR section shown in (g). (k) Image of overlapped maps to show chemical compositions. (l) EELS profile taken from a typical BNHNR.

strong sp^2-bonding, that is, the h-BN structure. Quantitative analysis of EELS spectra gives a B/N atomic ratio of 1.0 ± 0.1. No carbon was detected in the EELS profile, suggesting again that BNHNRs are pure BN, consistent with the EFTEM results.

To understand the optical properties of BNHNRs, Raman spectra were analyzed at room temperature. Figure 4a is the typical Raman spectrum of BNHNRs, which is similar to bulk h-BN as the dominant peak is centered at 1366 cm^{-1} and the reported bulk values are in the range of 1366−1370 cm^{-1}.[42,43] Recently, more convincing results show that the E_{2g} modes of a single crystal h-BN shift to lower wavelength because the interlayer interaction of h-BN sheets softens the sp^2 bonds in the bulk.[44] Our result (a shift to 1366 cm^{-1}) indicates the strong interlayer interactions of graphene-like sheets and high crystallinity in BNHNRs. More information of the lattice vibrations can be gained through Fourier transform infrared spectroscopy (FTIR) characterization. A typical result is presented in Figure 4b, which shows strong vibrations at 818 and 1367 cm^{-1}, indexed to the A_{2u} (BN vibration out-of-plane polarization) and E_{1u} (BN vibration in-plane polarization) mode, respectively. It is well-known that BN is a polar material where N is slightly negative-charged and B is slightly positive-charged. The long-range characteristics of the Coulomb potential gives rise to a macroscopic electric field *E* for longitudinal phonons, which results in a splitting between the longitudinal optical (LO) and transverse optical (TO) modes. In pyrolytic h-BN, the A_{2u} mode is split into A_{2u} (TO) and A2u (LO), with a shoulder at 767 cm^{-1} and a peak at 783 cm^{-1}, respectively, whereas the E_{1u} (TO) and E_{1u} (LO) modes are located at 1367 and 1510 cm^{-1}. These E_{2u} and E_{1u} phonons shift to 820 and 1366 cm^{-1},[45] or 800 and 1372 (1540) cm^{-1},[46] for multiwalled h-BN tubes, and 811 and 1377 (1514) cm^{-1} for polycrystalline h-BN.[46] For epitaxial monolayer of h-BN on metal surfaces, which shows a bucked structure with some sp^3 admixture, the modes show BN vibration at 790 and 1395 cm^{-1}.[47] For the as-prepared BNHNR, the E_{2u} is shifted to 818 cm^{-1} without any peak splitting, which is slightly higher than the reported h-BN materials. This can be explained by the lack of defects in the BN sheets that is responsible for the enhancement of IF responses and a hardening of the TO mode. The E_{1u} is shifted to 1367 cm^{-1} without obvious peak splitting, further indicating that the graphene-like BN sheet has higher crystallinity. To show the optical properties of BNHNRs for potential applications in blue laser and light emitting diodes, we measured the UV−vis absorption spectrum of the BNHNRs (Figure 4c). A narrow absorption line with the peak

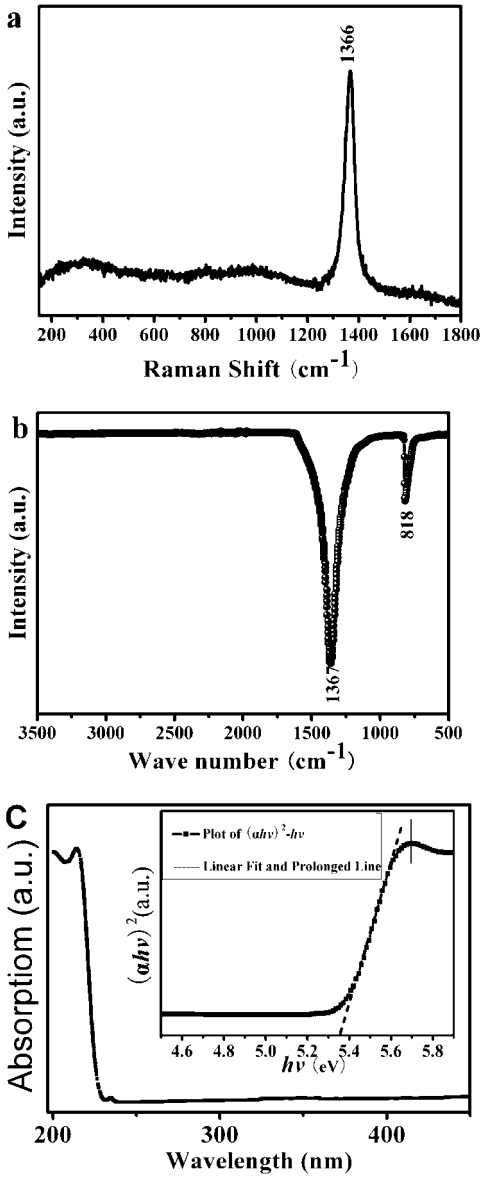

Figure 4. Raman (a), FTIR (b), and UV−vis (c) spectra of the synthesized BNHNRs.

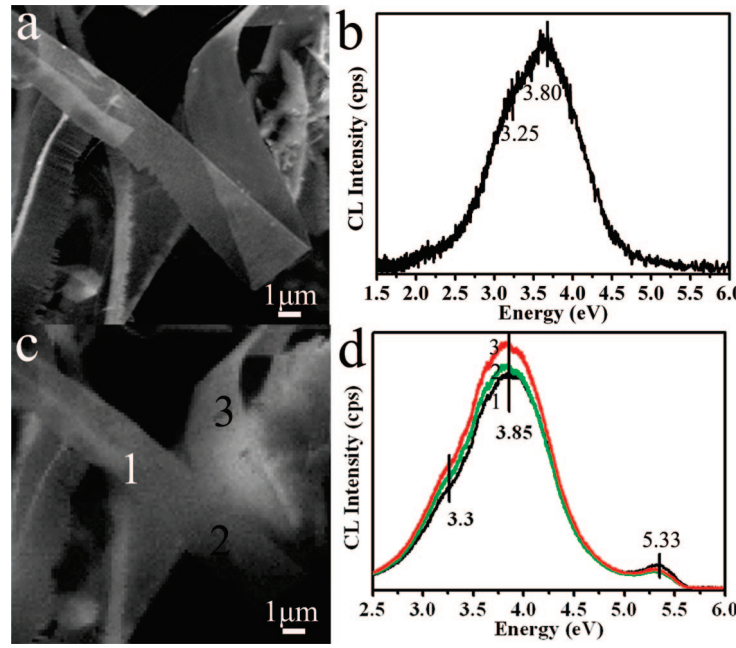

Figure 5. (a) SEM image of the BNHNR nanostructure on a copper grid; (b) CL spectrum taken at 300 K. (c) CL image at 336 nm showing the uniform contrast across the hollow belts. (d) CL spectra recorded at 20 K from three positions along the BNHNR nanostructure.

centered at 217 nm is observed, which corresponds to a band gap of ~5.67 eV. The energy is smaller than the reported one (centered at 6.15 eV) for h-BN micron-sized crystals. Such a shift in our BNHNR sample is attributed to the saddle point transition in the band structure of h-BN.[48] It is well-known that the relationship between the absorption coefficient (α) near the absorption edge and the optical band gap (E_g) for direct interband transitions obeys the following relation:[49]

$$(\alpha h\nu)^2 = A(h\nu - E_g)$$

where A is a parameter that relates to the effective mass associated with valence and conduction bands, and $h\nu$ is the photon energy. Hence, the band gap for the absorption edge can be obtained by extrapolating the linear portion of the plot $(\alpha h\nu)^2 - h\nu$ to $\alpha = 0$ from the inset of Figure 4c. From the inset, the optical absorption in the edge region can be well-fitted using a relation $(\alpha h\nu)^2 \sim (h\nu - E_g)$, confirming that the BNHNRs have a band gap of ~5.33 eV.

To further understand the optoelectronic properties of BNHNRs, their CL properties were determined. Figure 5a,b shows the SEM images of a BNHNR and its corresponding room temperature CL spectrum. The spectrum is basically composed of a relatively broad emission peak that can be deconvoluted into two peaks (centered at 3.25 and 3.80 eV). Similar observations[34,50,51] suggest that they can be attributed to the deep-level emissions associated with defect-related centers (B or N vacancy-type defect-trapped states). Han *et al.*[52] reported that the CL spectra between 3.0 and 4.2 eV are due to radiative transitions which could be generated by a replacement of some N atoms with O from the experimental and theoretical analysis. Figure 5c is its SEM-CL image taken at a wavelength of 336 nm and shows a uniform contrast, suggesting the uniform optical properties across the entire BNHNR. Figure 5d shows three CL spectra taken at three locations marked in Figure 5c at a temperature of 20 K, showing almost identical spectra. This indicates clearly that the BNHNRs are homogeneous in terms of the crystal structure and CL property. Compared with the emissions at room temperature, the two deep-level emissions are shifted by 0.05 eV, that is, from 3.25 to 3.30 eV and from 3.80 to 3.85 eV. In addition, a UV emission, centered at 5.33 eV, can be clearly observed. In addition, an UV emission, centered at 5.33 eV, can be clearly observed. This emission is similar to

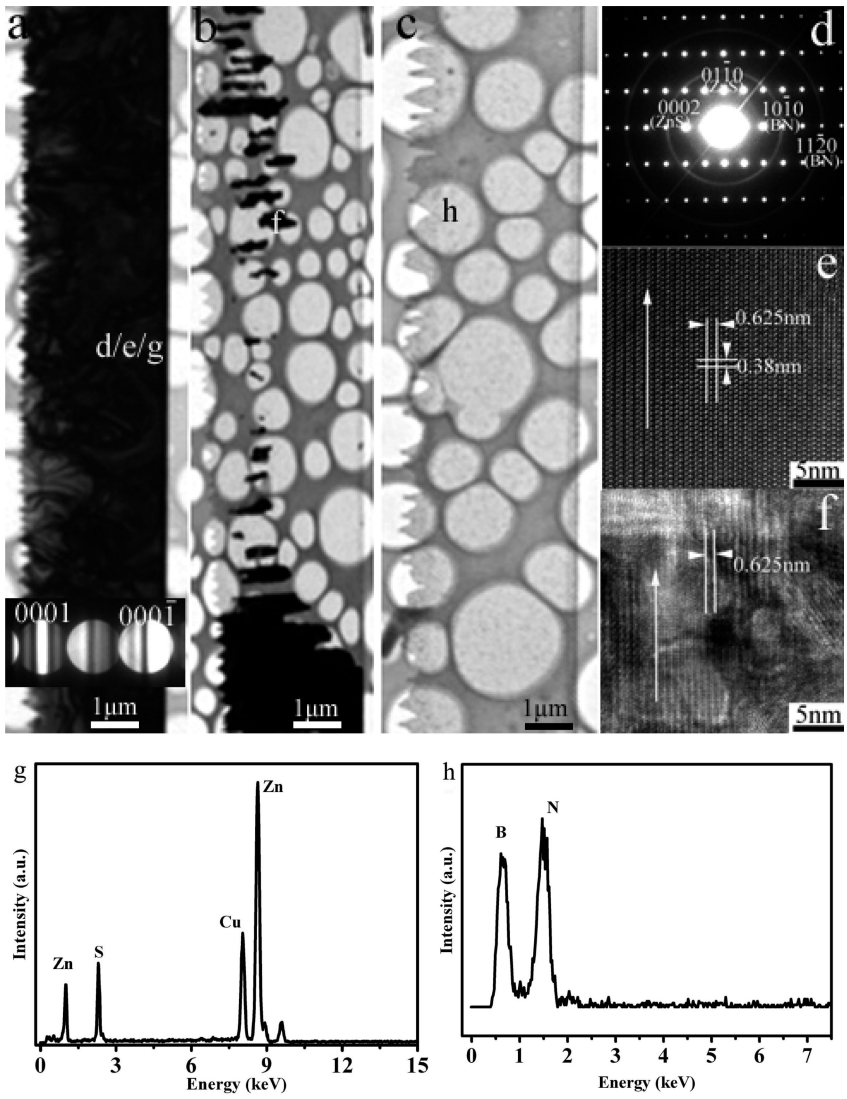

Figure 6. TEM images showing the initial, intermediate, and final stages of the replication process. (a) ZnS/BN core/shell nanostructure. (b) Intermediate stage of ZnS evaporation. (c) Final form of a section of BNHNR. (d) SAED pattern taken from middle of (a) showing the overlapped diffraction patterns of a ZnS single crystal and preferentially oriented BN honeycomb sheets. (e,f) HRTEM images taken from highly crystalline ZnS template (e) and being vaporized ZnS (f). (g,h) EDS profiles taken from a core−shell heterostructure (g) and a final replicated BNHNR nanostructure (h) confirming that the template ZnS and the replicated nanostructure BNHNR.

the observed near-band edge emission in the UV region,[53] but the value is less than the reported value (5.8 eV) for bulk h-BN.[54−56] Very recently, Jaffrennou *et al.*[57] recorded a luminescence around 230 nm (~5.38 eV) from multiwalled BNNTs, and they attributed it to excitonic effects, more precisely to excitons bound to the structural defects: dislocations and facets, which are observed along the walls. However, Han *et al.*[52] considered that the luminescence at 5.38 eV is a direct band gap emission of multiwalled BNNTs. Compared to the above results, the emission at 5.33 eV may be attributed to near band gap excitonic recombination in the structure of BNHNR. Other emissions have been often found in BN nanostructures, such as emission peak at 3.3 eV with a shoulder at 4.1 eV found in pure multiwalled BNNTs,[45] ~3.8 and ~1.8 eV in BN nanorods,[51] 3.0 eV with a shoulder at 2.8 eV in BN nanohorns,[34] and 3.26 and 2.88 eV in Eu-doped BN nanotubes.[58] Interestingly, the far UV emission of BN has been constantly observed in the well crystalline h-BN structures, such as microsized h-BN film[53] or bulk h-BN.[54] This suggests that the synthesized BNHNRs have high crystallinity and, in turn, exhibit extraordinary ultraviolet optoelectronic properties, which is essential for the optoelectronic applications in the ultraviolet region.

To understand the CL properties of the synthesized BNHNRs, the structural relationship between the replicated BNHNRs and ZnS templates was investigated in detail by TEM. Figure 6a−c is TEM images with typical starting, intermediate, and final nanostructures. Figure 6a is a TEM image consisting of a ZnS nanoribbon with a BN shell where the two long edges are shown different—one being zigzag and the other being straight. Convergent beam electron diffraction (CBED) study (as shown in inset of Figure 6a) of the ZnS nanoribbons suggests that the $[0001]_{ZnS}$ direction is toward the zigzag edge. Figure 6d is a SAED pattern taken from the middle region of Figure 6a, in which a single ZnS diffraction pattern has been superimposed with the BN diffraction pattern (as shown in Figure 3c). As can be seen from Figure 6d, two of the six arcs of $10\bar{1}0^*_{BN}$ are almost superimposed with $\pm 0003^*_{ZnS}$. Theoretical estimation suggests that there exists 3.8% lattice mismatch between $d_{10\bar{1}0}$(BN) and d_{0003}(ZnS). We anticipate that this small lattice mismatch is the driving force for replicated BN honeycomb sheets to be preferentially oriented with the crystal structure of the ZnS template. As a consequence, defined BN oriented sheets have been achieved, which results in an high crystallinity and, in turn, the extraordinary near-band-gap emission of the synthesized BNHNRs. Figure 6e,f is the HRTEM images taken from ZnS belts, with Figure 6e being in the middle region of Figure 6a and Figure 6f being the residual ZnS region of Figure 6b. This pair of HRTEM images suggests very high crystallinity of the initial ZnS templates and the rigorously degraded crystallinity during its vaporization. The chemical compositions of the template and replicated BNHNR nanostructures were studied using EDS, and the results are shown in Figure 6g (taken from the middle of Figure 6a) and Figure 6h (taken from the middle of Figure 6c), confirming that the template is ZnS and the replicated nanostructures is BN.

To test the generalization of this synthesis strategy, BCN hollow nanoribbons (BCNHNRs) were synthesized and characterized. For synthesizing BCN hollow nanoribbons, the flow of NH_3 was reduced to 25 sccm and the mixture gas went through a bottle containing benzene before entering the furnace. Figure 7a−c is the SEM/TEM images confirming that the synthesized product has a hollow structure. Figure 7d is a typical EELS profile and shows clearly the C edge, indicating that the synthesized product is B−C−N. Quantitative analysis of EELS spectra gives an atomic ratio of B/C/N = 1:0.29:1. To determine their chemical composition and the composition uniformity of the synthesized BCNHNRs, elemental maps of B, C, and N were performed with the energy loss windows centered, respectively, at the B *K* edge of 188 eV, the N *K* edge of 401 eV, and the C *K* edge of 284 eV, and with slit sizes of 10, 20, and 16 eV. Figure 7e is an image using electrons with the zero energy loss and shows the general morphology of a section of a BCNHNR. Figure 7f−h shows the B, C, and N maps of the section and show clearly the presence of B, C, and N. It should be noted that Figure 7g is a C map, in which the holey C film is clearly shown. However, the appearance of C signal in the BCNHNR section in Figure 7g suggests that the BCNHNR contains C. The fact that the decreased intensity in the overlapping region between the BCNHNR and C supporting film, compared with the area of pure C supporting film, can be explained as the result of the multiple scattering effect. Figure 7i is the overlapped image of B, C, and N maps, indicating that all constituting B, C, and N elements are homogeneously distributed in the hollow nanostructure.[59]

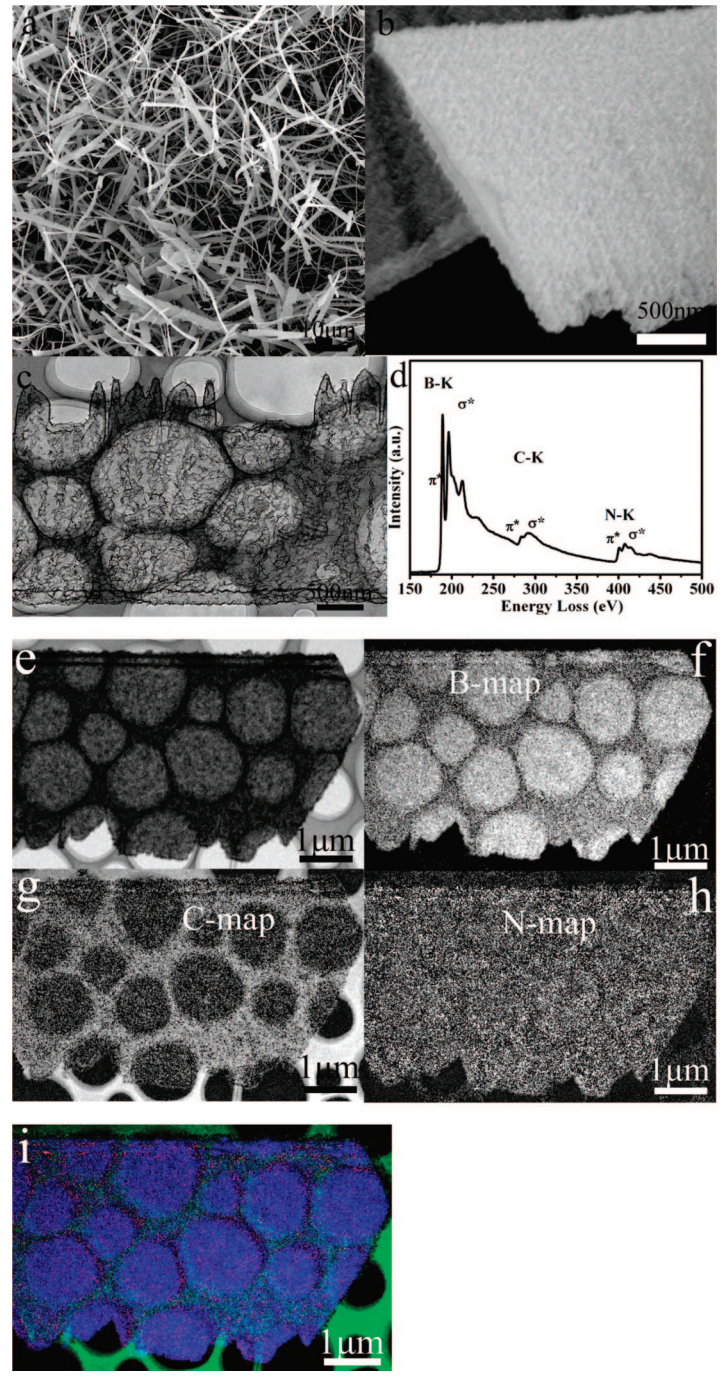

Figure 7. Typical SEM/TEM images showing general morphology of BCN nanostructures. (a) SEM image showing a high yield of synthesized belt-shaped nanostructures. (b) SEM image showing detailed morphology. (c) TEM image showing hollow characteristic. (d) EELS profile showing the C. (e) Zero-loss image of a section of a BCNHNR. (f−h) Elemental mappings (B, N, and C) of the BCNHNR section. (i) Overlapped maps to show chemical composition.

CONCLUSIONS

In conclusion, through a simple templating approach, we have synthesized novel BNHNRs. These novel BN nanostructures have distinct structural and optoelectronic characteristics when compared with other forms of BN nanostructures. With high crystallinity, the replicated BNHNRs demonstrate an ultraviolet CL property, which is critically important for their potential optoelectronic applications, particularly in the ultraviolet region. The success of extending this simple templating method to synthesize other hollow nanostructures, such as BCN hollow nanoribbons, suggests that the method can be adopted to fabricate many other hollow formed nanostructures.

METHODS

Synthesis of BN Hollow Nanostructures. A high temperature horizontal multizone tube furnace was used for the synthesis in this study. An alumina tube with an outer diameter of 32 mm and a length of 1 m was placed in the furnace. The BNHNRs were prepared using B−N−O−Fe and ZnS precursors by chemical vapor deposition (CVD) with high reproducibility. The nitrogen-rich B−N−O−Fe precursor was prepared by ball milling a mixture of B−O−Fe (mass ratio: $B/B_2O_3/Fe_2O_3$ = 1:7:2) under ammonia atmosphere for 1 h. One gram of B−N−O−Fe precursor and 1 g of ZnS powder were loaded into an alumina crucible at the center of the tube furnace. High purity Ar (at a rate of 150 sccm), NH_3 (at 75 sccm), and H_2 (at 20 sccm) were used as the carrier

and reaction gases, respectively. The furnace temperature was increased to 1220 °C at a rate of 35 °C min^{-1} and maintained at that temperature for 2 h to form ZnS/BN core/shell heterostructures. Subsequently, the reactor temperature was increased to 1350 °C and maintained for 4 h in vacuum at 50 Torr to remove ZnS template.

Structural Characterization. The synthesized products were comprehensively characterized using X-ray diffraction (XRD, RINT2200, Cu Kα), scanning electron microscopy (SEM, 6400F), transmission electron microscopy (TEM, Tecnai F30 equipped with electron energy loss spectroscopy (EELS) and energy-dispersive X-ray spectroscopy (EDS)), Raman spectroscopy (Labram HR 800 micro Raman system with Ar laser excited at 514.5 nm), Fourier transform infrared spectroscopy (FTIR, a Necolet 6700 FTIR spectrometer with a laser at 1024nm), and UV−vis spectrophotometer (JASCO-V550).

Cathodoluminescence (CL) Characterization. Spatially resolved CL measurements and *in situ* CL imaging of BNHNRs were carried out (TFE-SEM, Hitachi S4200). The samples were first deposited on a standard copper TEM grid and thoroughly characterized using TEM and were then used for CL characterization. CL spectra of BNHNRs were collected using a high resolution CL system operating at an accelerating voltage of 5 kV and a current of 1.2 nA.

Acknowledgment. This work was supported by the Key Research Program of MOST, China (2006CB932703) and Australian Research Council. The authors also thank to D. M. Tang, C Liu, X. L. Ma for kind assistance and discussion.

REFERENCES AND NOTES

1. Iijima, S. Helical Microtubules of Graphitic Carbon. *Nature* **1991**, *354*, 56–58.
2. Dekker, C. Carbon Nanotubes as Molecular Quantum Wires. *Phys. Today* **1999**, *52*, 22–28.
3. Tenne, R. Inorganic Nanotubes and Fullerene-Like Nanoparticles. *Nat. Nanotechnol.* **2006**, *1*, 103–111.
4. Goldberger, J.; Fan, R.; Yang, P. D. Inorganic Nanotubes: A Novel Platform for Nanofluidics. *Acc. Chem. Res.* **2006**, *39*, 239–248.
5. Hu, J. Q.; Li, Q.; Zhan, J. H.; Jiao, Y.; Liu, Z. W.; Ringer, S. P.; Bando, Y.; Golberg, D. Unconventional Ribbon-Shaped Beta-Ga_2O_3 Tubes with Mobile Sn Nanowire Fillings. *ACS Nano* **2008**, *2*, 107–112.
6. Chen, Z. G.; Li, F.; Ren, W. C.; Cong, H. T.; Liu, C.; Lu, G. Q.; Cheng, H. M. Double-Walled Carbon Nanotubes Synthesized Using Carbon Black as the Dot Carbon Source. *Nanotechnology* **2006**, *17*, 3100–3104.
7. Dai, H. J.; Wong, E. W.; Lu, Y. Z.; Fan, S. S.; Lieber, C. M. Synthesis and Characterization of Carbide Nanorods. *Nature* **1995**, *375*, 769–772.
8. Pan, Z. W.; Dai, Z. R.; Wang, Z. L. Nanobelts of Semiconducting Oxides. *Science* **2001**, *291*, 1947–1949.
9. Chen, Z. G.; Li, F.; Liu, G.; Tang, Y. B.; Cong, H. T.; Lu, G. Q.; Cheng, H. M. Preparation of High Purity ZnO Nanobelts by Thermal Evaporation of ZnS. *J. Nanosci. Nanotechnol.* **2006**, *6*, 704–707.
10. Hafner, J. H.; Cheung, C. L.; Lieber, C. M. Growth of Nanotubes for Probe Microscopy Tips. *Nature* **1999**, *398*, 761–762.
11. Mitchell, D. T.; Lee, S. B.; Trofin, L.; Li, N. C.; Nevanen, T. K.; Soderlund, H.; Martin, C. R. Smart Nanotubes for Bioseparations and Biocatalysis. *J. Am. Chem. Soc.* **2002**, *124*, 11864–11865.
12. Han, W. Q.; Zettl, A. Functionalized Boron Nitride Nanotubes with a Stannic Oxide Coating: A Novel Chemical Route to Full Coverage. *J. Am. Chem. Soc.* **2003**, *125*, 2062–2063.
13. Ugarte, D.; Chatelain, A.; deHeer, W. A. Nanocapillarity and Chemistry in Carbon Nanotubes. *Science* **1996**, *274*, 1897–1899.
14. Kongkanand, A.; Kamat, P. V. Electron Storage in Single Wall Carbon Nanotubes. Fermi Level Equilibration in Semiconductor-SWCNT Suspensions. *ACS Nano* **2007**, *1*, 13–21.
15. Martin, C. R. Nanomaterials: A Membrane-Based Synthetic Approach. *Science* **1994**, *266*, 1961–1966.
16. Brumlik, C. J.; Martin, C. R. Template Synthesis of Metal Microtubules. *J. Am. Chem. Soc.* **1991**, *113*, 3174–3175.
17. Goldberger, J.; He, R. R.; Zhang, Y. F.; Lee, S. W.; Yan, H. Q.; Choi, H. J.; Yang, P. D. Single-Crystal Gallium Nitride Nanotubes. *Nature* **2003**, *422*, 599–602.
18. Martin, C. R. Template Synthesis of Electronically Conductive Polymer Nanostructures. *Acc. Chem. Res.* **1995**, *28*, 61–68.
19. Miller, S. A.; Young, V. Y.; Martin, C. R. Electroosmotic Flow in Template-Prepared Carbon Nanotube Membranes. *J. Am. Chem. Soc.* **2001**, *123*, 12335–12342.
20. Pu, Y. C.; Hwu, J. R.; Su, W. C.; Shieh, D. B.; Tzeng, Y.; Yeh, C. S. Water-Dissolvable Sodium Sulfate Nanowires as a Versatile Template for the Fabrication of Polyelectrolyte- and Metal-Based Nanotubes. *J. Am. Chem. Soc.* **2006**, *128*, 11606–11611.
21. Lee, H. Y.; Nam, S. R.; Hong, J. I. Microtubule Formation Using Two-Component Gel System. *J. Am. Chem. Soc.* **2007**, *129*, 1040–1041.
22. Yin, Y. D.; Rioux, R. M.; Erdonmez, C. K.; Hughes, S.; Somorjai, G. A.; Alivisatos, A. P. Formation of Hollow Nanocrystals through the Nanoscale Kirkendall Effect. *Science* **2004**, *304*, 711–714.
23. Blase, X.; Rubio, A.; Louie, S. G.; Cohen, M. L. Stability and Band-Gap Constancy of Boron-Nitride Nanotubes. *Europhys. Lett.* **1994**, *28*, 335–340.
24. Golberg, D.; Bando, Y.; Tang, C. C.; Zhi, C. Y. Boron Nitride Nanotubes. *Adv. Mater.* **2007**, *19*, 2413–2432.
25. Golberg, D.; Costa, P.; Lourie, O.; Mitome, M.; Bai, X. D.; Kurashima, K.; Zhi, C. Y.; Tang, C. C.; Bando, Y. Direct Force Measurements and Kinking under Elastic Deformation of Individual Multiwalled Boron Nitride Nanotubes. *Nano Lett.* **2007**, *7*, 2146–2151.
26. Han, W. Q.; Mickelson, W.; Cumings, J.; Zettl, A. Transformation of $B_xC_yN_z$ Nanotubes to Pure BN Nanotubes. *Appl. Phys. Lett.* **2002**, *81*, 1110–1112.
27. Chen, Y.; Zou, J.; Campbell, S. J.; Le Caer, G. Boron Nitride Nanotubes: Pronounced Resistance to Oxidation. *Appl. Phys. Lett.* **2004**, *84*, 2430–2432.
28. Golberg, D.; Bando, Y.; Kurashima, K.; Sato, T. Synthesis and Characterization of Ropes Made of BN Multiwalled Nanotubes. *Scripta Mater.* **2001**, *44*, 1561–1565.
29. Mele, E. J.; Kral, P. Electric Polarization of Heteropolar Nanotubes as a Geometric Phase. *Phys. Rev. Lett.* **2002**, *88*, 05680-3–056803-4.
30. Chopra, N. G.; Luyken, R. J.; Cherrey, K.; Crespi, V. H.; Cohen, M. L.; Louie, S. G.; Zettl, A. Boron-Nitride Nanotubes. *Science* **1995**, *269*, 966–967.
31. Chen, Z.-G.; Zou, J.; Liu, Q.; Sun, C.; Liu, G.; Yao, X.; Li, F.; Wu, B.; Yuan, X.-L.; Sekiguchi, T.; et al. Self-Assembly and Cathodoluminescence of Microbelts from Cu-Doped Boron Nitride Nanotubes. *ACS Nano* **2008**, *2*, 1523–1532.
32. Ma, R. Z.; Bando, Y.; Sato, T. Controlled Synthesis of BN Nanotubes, Nanobamboos, and Nanocables. *Adv. Mater.* **2002**, *14*, 366–368.
33. Chen, Z. G.; Zou, J.; Li, F.; Liu, G.; Tang, D. M.; Li, D.; Liu, C.; Ma, X. L.; Cheng, H. M.; Lu, G. Q.; et al. Growth of Magnetic Yard-Glass Shaped Boron Nitride Nanotubes with Periodic Iron Nanoparticles. *Adv. Funct. Mater.* **2007**, *17*, 3371–3376.
34. Zhi, C. Y.; Bando, Y.; Tang, C. C.; Golberg, D.; Xie, R. G.; Sekiguchi, T. Large-Scale Fabrication of Boron Nitride Nanohorn. *Appl. Phys. Lett.* **2005**, *87*, 63107–63109.
35. Huo, K. F.; Hu, Z.; Chen, F.; Fu, J. J.; Chen, Y.; Liu, B. H.; Ding, J.; Dong, Z. L.; White, T. Synthesis of Boron Nitride Nanowires. *Appl. Phys. Lett.* **2002**, *80*, 3611–3613.
36. Chen, Z. G.; Zou, J.; Lu, G. Q.; Liu, G.; Li, F.; Cheng, H. M. ZnS Nanowires and Their Coaxial Lateral Nanowire Heterostructures with BN. *Appl. Phys. Lett.* **2007**, *90*, 103117–103120.
37. Ma, C.; Moore, D.; Li, J.; Wang, Z. L. Nanobelts, Nanocombs, and Nanowindmills of Wurtzite ZnS. *Adv. Mater.* **2003**, *15*, 228–231.

38. Chen, Z. G.; Zou, J.; Liu, G.; Lu, H. F.; Li, F.; Cheng, H. M.; Lu, G. Q. Silicon-Induced Oriented ZnS Nanobelts for Hydrogen Sensitivity. *Nanotechnology* **2008**, *19*, 055710.
39. Moore, D.; Wang, Z. L. Growth of Anisotropic One-Dimensional ZnS Nanostructures. *J. Mater. Chem.* **2006**, *16*, 3898–3905.
40. Wang, Z. W.; Daemen, L. L.; Zhao, Y. S.; Zha, C. S.; Downs, R. T.; Wang, X. D.; Wang, Z. L.; Hemley, R. J. Morphology-Tuned Wurtzite-Type ZnS Nanobelts. *Nat. Mater.* **2005**, *4*, 922–927.
41. Jiang, Y.; Meng, X. M.; Liu, J.; Xie, Z. Y.; Lee, C. S.; Lee, S. T. Hydrogen-Assisted Thermal Evaporation Synthesis of ZnS Nanoribbons on a Large Scale. *Adv. Mater.* **2003**, *15*, 323–327.
42. Hoffman, D. M.; Doll, G. L.; Eklund, P. C. Optical Properties of Pyrolytic Boron Nitride in the Energy Range 0.05−10 eV. *Phys. Rev. B* **1984**, *30*, 6051–6056.
43. Geick, R.; Perry, C. H.; Rupprecht, G. Normal Modes in Hexagonal Boron Nitride. *Phys. Rev.* **1966**, *146*, 543–547.
44. Arenal, R.; Ferrari, A. C.; Reich, S.; Wirtz, L.; Mevellec, J. Y.; Lefrant, S.; Rubio, A.; Loiseau, A. Raman Spectroscopy of Single-Wall Boron Nitride Nanotubes. *Nano Lett.* **2006**, *6*, 1812–1816.
45. Zhi, C. Y.; Bando, Y.; Tang, C. C.; Golberg, D.; Xie, R. G.; Sekigushi, T. Phonon Characteristics and Cathodoluminescence of Boron Nitride Nanotubes. *Appl. Phys. Lett.* **2005**, *86*, 213110-1–213110-3.
46. Borowiak-Palen, E.; Pichler, T.; Fuentes, G. G.; Bendjemil, B.; Liu, X.; Graff, A.; Behr, G.; Kalenczuk, R. J.; Knupfer, M.; Fink, J. Infrared Response of Multiwalled Boron Nitride Nanotubes. *Chem. Commun.* **2003**, 82–83.
47. Rokuta, E.; Hasegawa, Y.; Suzuki, K.; Gamou, Y.; Oshima, C.; Nagashima, A. Phonon Dispersion of an Epitaxial Monolayer Film of Hexagonal Boron Nitride on Ni(111). *Phys. Rev. Lett.* **1997**, *79*, 4609–4612.
48. Zunger, A.; Katzir, A.; Halperin, A. Optical Properties of Hexagonal Boron Nitride. *Phys. Rev. B* **1976**, *13*, 5560–5573.
49. Peng, X. S.; Meng, G. W.; Zhang, J.; Zhao, L. X.; Wang, X. F.; Wang, Y. W.; Zhang, L. D. Electrochemical Fabrication of Ordered Bi_2S_3 Nanowire Arrays. *J. Phys. D: Appl. Phys.* **2001**, *34*, 3224–3228.
50. Lauret, J. S.; Arenal, R.; Ducastelle, F.; Loiseau, A.; Cau, M.; Attal-Tretout, B.; Rosencher, E.; Goux-Capes, L. Optical Transitions in Single-Wall Boron Nitride Nanotubes. *Phys. Rev. Lett.* **2005**, *94*, 037405.
51. Zhang, H. Z.; Phillips, M. R.; Fitzgerald, J. D.; Yu, J.; Chen, Y. Patterned Growth and Cathodoluminescence of Conical Boron Nitride Banorods. *Appl. Phys. Lett.* **2006**, *88*, 093117–093119.
52. Han, W. Q.; Yu, H. G.; Zhi, C.; Wang, J.; Liu, Z.; Sekiguchi, T.; Bando, Y. Isotope Effect on Band Gap and Radiative Transitions Properties of Boron Nitride Nanotubes. *Nano Lett.* **2008**, *8*, 491–494.
53. Taylor, C. A.; Brown, S. W.; Subramaniam, V.; Kidner, S.; Rand, S. C.; Clarke, R. Observation of Near-Band-Gap Luminescence from Boron-Nitride Films. *Appl. Phys. Lett.* **1994**, *65*, 1251–1253.
54. Watanabe, K.; Taniguchi, T.; Kanda, H. Direct-Bandgap Properties and Evidence for Ultraviolet Lasing of Hexagonal Boron Nitride Single Crystal. *Nat. Mater.* **2004**, *3*, 404–409.
55. Watanabe, K.; Taniguchi, T.; Kuroda, T.; Kanda, H. Effects of Deformation on Band-Edge Luminescence of Hexagonal Boron Nitride Single Crystals. *Appl. Phys. Lett.* **2006**, *89*, 141902–141904.
56. Kubota, Y.; Watanabe, K.; Tsuda, O.; Taniguchi, T. Deep Ultraviolet Light-Emitting Hexagonal Boron Nitride Synthesized at Atmospheric Pressure. *Science* **2007**, *317*, 932–934.
57. Jaffrennou, P.; Barjon, J.; Schmid, T.; Museur, L.; Kanaev, A.; Lauret, J. S.; Zhi, C. Y.; Tang, C.; Bando, Y.; Golberg, D.; et al. Near-Band-Edge Recombinations in Multiwalled Boron Nitride Nanotubes: Cathodoluminescence and Photoluminescence Spectroscopy Measurements. *Phys. Rev. B* **2008**, *77*, 235422-1–235422-7.
58. Chen, H.; Chen, Y.; Li, C. P.; Zhang, H. Z.; Williams, J. S.; Liu, Y.; Liu, Z. W.; Ringer, S. P. Eu-Doped Boron Nitride Nanotubes as a Nanometer-Sized Visible-Light Source. *Adv. Mater.* **2007**, *19*, 1845–1848.
59. Golberg, D.; Dorozhkin, P. S.; Bando, Y.; Mitome, M.; Tang, C. C. Discrimination of B−C−N Nanotubes through Energy-Filtering Electron Microscopy. *Diam. Relat. Mater.* **2005**, *14*, 1857–1866.